

# Phonons and Quantum criticality revealed by temperature linear resistivity in twisted double bilayer graphene

Yanbang Chu<sup>1,2</sup>, Le Liu<sup>1,2</sup>, Cheng Shen<sup>1,2</sup>, Jinpeng Tian<sup>1,2</sup>, Jian Tang<sup>1,2</sup>, Yanchong Zhao<sup>1,2</sup>, Jieying Liu<sup>1,2</sup>, Yalong Yuan<sup>1,2</sup>, Yiru Ji<sup>1,2</sup>, Rong Yang<sup>1,3,4</sup>, Kenji Watanabe<sup>5</sup>, Takashi Taniguchi<sup>6</sup>, Dongxia Shi<sup>1,2,3,4</sup>, Fengcheng Wu<sup>7</sup>, Wei Yang<sup>1,2,3,4\*</sup>, Guangyu Zhang<sup>1,2,3,4\*</sup>

<sup>1</sup> *Beijing National Laboratory for Condensed Matter Physics, Institute of Physics, Chinese Academy of Sciences, Beijing 100190, China*

<sup>2</sup> *School of Physical Sciences, University of Chinese Academy of Sciences, Beijing, 100190, China*

<sup>3</sup> *Beijing Key Laboratory for Nanomaterials and Nanodevices, Beijing 100190, China*

<sup>4</sup> *Songshan Lake Materials Laboratory, Dongguan, Guangdong, 523808, China*

<sup>5</sup> *Research Center for Functional Materials, National Institute for Materials Science, 1-1 Namiki, Tsukuba 305-0044, Japan*

<sup>6</sup> *International Center for Materials Nanoarchitectonics, National Institute for Materials Science, 1-1 Namiki, Tsukuba 305-0044, Japan*

<sup>7</sup> *School of Physics and Technology, Wuhan University, Wuhan 430072, China*

\*Corresponding authors: [wei.yang@iphy.ac.cn](mailto:wei.yang@iphy.ac.cn); [gzhang@iphy.ac.cn](mailto:gzhang@iphy.ac.cn)

## Abstract

Twisted double bilayer graphene (TDBG) is an electric-field-tunable moiré system, exhibiting electron correlated states and related temperature linear (T-linear) resistivity. The displacement field provides a new knob to in-situ tune the relative strength of electron interactions in TDBG, yielding not only a rich phase diagram but also the ability to investigate each phase individually. Here, we report a study of carrier density ( $n$ ), displacement field ( $D$ ) and twist angle ( $\theta$ ) dependence of T-linear resistivity in TDBG. For a large twist angle ( $\theta > 1.5^\circ$ ) where correlated insulating states are absent, we observe a T-linear resistivity (order of  $10\Omega/K$ ) over a wide range of carrier density and its slope decreases with increasing of  $n$ , in agreement with acoustic phonon scattering model qualitatively and quantitatively. The slope of T-linear resistivity is non-monotonically dependent on displacement field, with a single peak structure closely connected to single-particle van Hove Singularity in TDBG. For an optimal twist angle of  $\sim 1.23^\circ$  in the presence of correlated states, the slope of T-linear resistivity is found maximum at the boundary of the correlated halo regime (order of  $100\Omega/K$ ), resulting in a “M” shaped displacement field dependence. The observation is beyond the phonon scattering model from single particle picture, and instead it suggests a quantum critical behavior. We interpret the observation as a result of symmetry-breaking instability developed at quantum critical points where electron degeneracy changes. Our results demonstrate that TDBG is an ideal system to study the interplay between phonon and quantum criticality, and might help to map out the evolution of the order parameters for the ground states.

## Introduction

Resistivity ( $R$ ) is a measure of how electrons are transported and scattered in solids, and it gives rich and fundamental information of the given system. It usually shows a power law dependence on temperature ( $T$ ),  $R \propto T^\alpha$ , where  $\alpha$  is a coefficient that differs from one scattering mechanism to another. Of particular interest is linear regime when  $\alpha = 1$ , since it could originate from conventional acoustic phonon couplings (Fig. 1a)<sup>1</sup>, but also it might indicate unconventional processes that rooted in quantum criticality<sup>2-4</sup> (Fig. 1b). The latter strange metal behaviors are observed in a wide range of correlated systems, for instance cuprates<sup>5</sup>, iron-based compounds<sup>6,7</sup>, heavy fermion systems<sup>8,9</sup>, Kondo lattices<sup>10</sup>, and frustrated lattices<sup>11,12</sup>, where quantum critical points are found with the instabilities of order parameters. So far, most studies focus on individual states and are limited by in-situ sample tunability, research on the critical behavior near critical points is still lacking yet.

Twisted moiré superlattice has emerged as a new platform for hosting rich correlated states. In twisted bilayer graphene (TBG), the generation of low energy flat bands<sup>13</sup> quenches kinetic energy of electrons and brings about correlated insulating states<sup>14</sup>, superconductivity<sup>15-17</sup>, ferromagnetism<sup>18,19</sup>. Large temperature linear (T-linear) resistivity has also been observed in TBG<sup>20,21</sup>, which bears a lot of similarity with that in optimally doped cuprates<sup>22</sup>. While the experiments in ref.20 support the electron phonon (el-ph) scattering model<sup>23</sup>, those in ref.21 are in favor of strange metal behavior with near Planckian dissipation in magic angle TBG, leaving the origin of the T-linear resistivity in TBG still elusive. In twisted double bilayer graphene (TDBG), another graphene-based twisted 2D material system, observations of halo structures and spin-polarized correlated insulating state, as well as T-linear resistivity, have been reported<sup>24-27</sup>. The previous reports are mainly focused on the  $R(T)$  curves in the nonlinear regime where  $R$  rapidly drops at low  $T$ , and the linear behaviors at high  $T$  are observed yet barely explored, demanding an in-depth and systematic exploration.

Compared to TBG, TDBG is more advantaged in tuning electron interactions, aside from twist angle. This is achieved by in-situ tuning of displacement field, which changes the flat bandwidth  $W$  and band separation  $\Delta$  in the band structure of TDBG<sup>28</sup>. The displacement field acts as an extra parameter to control the relative strength of electron interactions to kinetic energy. This not only contributes a versatile phase diagram, but also allows an in-situ switch between different phases in TDBG, avoiding variation between different samples. Meanwhile, with temperature scaling of resistivity as the probe, one can elucidate the dominating scattering mechanism, and then evaluate the relative importance of electron-phonon coupling or electron interaction at low temperature where correlated states emerge and switch<sup>20,29</sup>.

In this work, we systematically study T-linear resistivity in TDBG. We found T-linear resistivity in a wide range of twist angle, from ‘optimal’ twist angle  $1.23^\circ$  to relatively larger twist angle  $1.91^\circ$ . We first start with a large twist angle device where correlated insulating states are absent, and find the dominating role played by acoustic phonons for the T-linear resistivity. Meanwhile, we also demonstrate a displacement field tunable electron-phonon interaction and its intimate connection with van Hove Singularity (vHS). And then in the ‘optimal’ twist angle devices, we reveal and highlight the features beyond the phonon model, and discuss the role played by quantum criticality in TDBG.

## Results

**Device information.** The TDBG samples are prepared by ‘cut and stack’ technique<sup>30</sup>, encapsulated by top and bottom hBN flakes, and then they are deposited on SiO<sub>2</sub>/Si substrate. The devices are designed with a dual gate Hall bar geometry and are fabricated in bubble-free region of the samples (see Methods for details). The dual gate geometry enables us to tune carrier density ( $n$ ) and electric displacement field ( $D$ ) independently, via carrier density  $n = (C_{BG}V_{BG} + C_{TG}V_{TG})/e$  and displacement field  $D = (C_{BG}V_{BG} - C_{TG}V_{TG})/2$ , where  $C_{BG}$  and  $C_{TG}$  are the geometrical capacitance per area for bottom and top dielectric layer,  $V_{BG}$  and  $V_{TG}$  are the bottom and top gate voltage, and  $e$  is the elementary charge. All our devices have length-to-width ratios close to one, with a twist angle  $\theta$  of 1.23°, 1.33°, 1.42°, 1.55° and 1.91°.

Figure 2a show the resistance as a function of  $n$  and  $D$  at a temperature of 1.8K in 1.55° device. There are three prominent resistance peaks, corresponding to charge neutral point (CNP) and superlattice gaps on both electron (+ $n_s$ ) and hole (- $n_s$ ) branches, as labelled in Fig.2a. Here,  $n_s = 4/A \approx 8\theta^2/\sqrt{3}a^2$  is the carrier density at full filling of a moiré unit cell and from which twist angle  $\theta$  can be determined, where  $a$  is the lattice constant of graphene and a prefactor of 4 comes from the valley and spin degeneracy in TDBG mini-Brillouin zone. Then moiré filling factor  $\nu = 4n/n_s$  is the number of carriers in one moiré unit cell. For an optimal twist angle of 1.23°, correlated insulating states (CI) are observed at half filling of conduction moiré subband and surrounded by halo structure in Fig.3a, consistent with previous works<sup>24-27</sup>. While for 1.55°, the correlated behavior is absent even though the displacement field is widely tuned, as shown in Fig.2a. Continuum model gives the displacement field tunable band structure of TDBG (Fig. S1 and S2), qualitatively consistent with experimental observations. We observe T-linear resistance in a wide range of twist angle,  $n$ , and  $D/\varepsilon_0$ , as shown in Fig. S3-S5, Fig. 2 and Fig. 3. The T-linear resistivity can be captured by  $R = A_1 T + R_0$ , where  $A_1$  is the linear slope and  $R_0$  is the residual resistance. It’s worth noting that the linear slope changes with  $n$ ,  $D$ , and  $\theta$ , which we explain in the following.

**T-linear resistivity and electron-phonon interaction at zero displacement field.** We first focus on 1.55° device in Fig.2 where correlated states are absent at low temperature of 1.8K. Fig.2b shows the  $R(T)$  curves for fillings  $\nu$  from 0.5 to 2.5 at  $D/\varepsilon_0=0$  V/nm, with the linear behaviors clearly demonstrated. The corresponding linear slope  $A_1(n)$ , about 10-30  $\Omega/K$ , are extracted and shown as a dark blue solid line in Fig.2c, and it follows a  $1/n$  dependence (Fig. S6c). Note that similar behavior is observed in 1.91° device, where  $A_1$  decreases with increasing  $\nu$ , despite of the overall smaller magnitude (Fig. S7a). Normalized  $A_1$  shows similar  $\nu$  dependence (Fig. S7b) in these two devices, suggesting the same origin of T-linear resistance.

We attribute the T-linear resistivity in these devices to the electron-phonon interactions in TDBG. Electrons traveled in metal are subjected to scattering from phonons, yielding a power law dependence of resistance on temperature. In monolayer graphene<sup>31</sup>, it follows a linear dependence at a high temperature,  $R(T) \sim T$ , and a superlinear dependence at a low temperature of Bloch-Grüneisen regime,  $R(T) \sim T^4$  (or  $\rho(T) \sim T^3$  in dirty sample where super-collisions of electron-phonon-impurity interactions dominate<sup>32,33</sup>). According to a theoretical calculation of electron-phonon scattering in TDBG<sup>34</sup>, acoustic phonon scattering is enhanced by reduced Fermi velocity in TDBG moiré subband. And it predicts a similar crossover from  $T$  at high temperature to  $T^4$  at low temperature ( $T < 10K$ ). If one take electron-electron Umklapp scattering<sup>35</sup>, it is more likely  $T^2$  when phonon occupation number is vanishing at low temperature. In the linear regime, the slope  $A_1$  resulted from acoustic phonon

scattering is given by<sup>34</sup>

$$A_1 = \frac{\pi U^2 k_B z_\infty}{2g_s g_v e^2 \hbar \rho_m v_{ph}^2 v_F^2} \quad (1)$$

where  $g_s, g_v$  are spin and valley degeneracies  $\rho_m$  is the mass density,  $U$  is acoustic phonon deformation potential,  $v_{ph}$  and  $v_F$  are phonon velocity and Fermi velocity,  $z_\infty$  is the integral concerning phonon occupation and other scattering details in TDBG. This model predicts a strong carrier density dependence for a parabolic dispersion, which yields  $v_F \sim k_F$  and thus results in  $dR/dT \propto 1/n$ .

Our experimental data are captured quantitatively by the above mentioned el-ph model. We plot the simulated  $A_1$  of T-linear resistivity to carrier density as the orange dashed line in Fig.2c, using  $\rho_m = 7.6 \times 10^{-7} \text{ kg/m}^2$ ,  $v_{ph} = 2.1 \times 10^4 \text{ m/s}$ ,  $U = 21 \text{ eV}$ ,  $z_\infty = 1.5$ , and  $v_F = \sqrt{(\hbar^2 n \pi / 2) / m^*}$  with  $m^* = 1.77 \times 10^{-34} \text{ kg}$ . We set an error bar of 40% due to the uncertainty of deformation potential  $U$  and effective mass. The simulated  $A_1$  and our observed one in Fig. 2c are in good agreement quantitatively. Besides, the onset temperature of T-linear resistivity is on the order of 1/4 Bloch-Grüneisen temperature (Fig. S8), which also agrees with the phonon model<sup>34</sup>.

**Deviation from 1/n dependence.** The actual band dispersion of TDBG is density as well as electric-field dependent. Therefore,  $A_1$  can deviate from the 1/n density dependence. For instance,  $A_1$  is found linear with  $1/\sqrt{n}$  for  $1.55^\circ$  devices at  $D/\varepsilon_0 = -0.45 \text{ V/nm}$  as well as  $1.91^\circ$  devices at  $D/\varepsilon_0 = 0$  and  $-0.4 \text{ V/nm}$  in Fig. S6. Besides,  $A_1$  is found minimum at around CNP and maximum next to band edges at full filling for  $1.23^\circ$  devices at  $D/\varepsilon_0 = 0 \text{ V/nm}$  in Fig. S9a, yet it follows a  $1/(n_s - n)$  dependence (Fig. S6e, g). These contrasts might indicate a renormalized parabolic band in TDBG, leading to  $v_F^2 \propto \sqrt{n}$  or  $v_F^2 \propto 1/(n_s - n)$  under certain conditions. Lastly, van Hove Singularity (vHS) can also change the Fermi surface and results in a deviation of  $A_1$  from 1/n dependence. The vHS by continuum model<sup>25</sup> in TDBG shows up as a cross-like feature in the phase diagram of  $R(n, D)$ , indicated by the black dashed lines in Fig.2f and Fig.3a. The upturn of  $A_1$  at around  $v=2$  for  $1.55^\circ$  device at  $D/\varepsilon_0 = -0.45 \text{ V/nm}$  (orange dash line in Fig. S7a) is consistent with the weak cross-like feature. Despite these complications, the above-mentioned T-linear resistivity that shows carrier density dependence other than 1/n, can still be captured within the framework of acoustic phonon scattering by taking non-parabolic band into account, and we name it ‘conventional metal’ (M).

**Field tunable electron phonon interactions.** We can deliberately change the band dispersion while keep carrier density  $n$  unchanged by applying displacement field  $D$ . It is thus expected to observe a change of T-linear resistivity when the applied field  $D$  is varied. Fig.2d shows the  $R(T)$  curves at  $v = 2$  for different field  $D/\varepsilon_0$  from 0 to  $-0.7 \text{ V/nm}$  in  $1.55^\circ$  device, with the linear behaviors well preserved. Figure 2e summarizes the curves of extracted  $A_1$  to  $D/\varepsilon_0$  at different  $v$ , and clearly it shows a non-monotonical and strong dependence that peaks on finite  $D/\varepsilon_0$ . As indicated by the arrow in Fig. 2e, the peak position (yellow dots in Fig. 2f) in  $D/\varepsilon_0$  shifts with moiré band filling factor  $v$  linearly, in parallel with resistance peak (black dashed line) in Fig. 2f. The resistance peak is reminiscent of the cross-like feature due to vHS in band structure, which might point to a close connection between T-linear resistance to the vHS. The field dependent  $A_1$  suggests a field tunable Fermi velocity or more fundamentally a tunable moiré band dispersion in TDBG, in agreement with the calculated field tunable moiré bandwidth (Fig. S1). However, there remains one puzzle regarding the offset between

yellow dots and the black dashed lines, as the band should be flattest at vHS and thus contribute a  $A_1$  peak according to the acoustic phonon scenario. The puzzle will be revisited later in this paper.

**Maximized T-linear resistivity at boundaries of halo structure.** We turn to the  $1.23^\circ$  device in Fig. 3a where correlated insulator and symmetry broken halo structure emerges at low temperature. Here, we focus on the field dependence of  $A_1$ . Fig.3b and 3c show the  $R(T)$  curves at fixed carrier density with  $v=2$  and  $1.8$ , respectively, with  $D/\varepsilon_0$  varied from  $-0.1$  to  $-0.6$  V/nm. Taking  $v=2$  for example, the field dependent  $A_1$  is extracted as red dots in Fig.3d. Similar to the results from  $1.55^\circ$  and  $1.91^\circ$  devices,  $A_1$  is strongly field tunable yet with a much larger magnitude. Moreover, the non-monotonical dependent  $A_1 (D/\varepsilon_0)$  shows two peaks in Fig. 3d, unlike the one peak in Fig. 2e. The “M” shaped two peaks are further confirmed by the numerical derivative  $dR/dT$  at  $T=20$  K in Fig. S10. More data at different filling  $v$  are shown in Fig. S11. These two peaks show different strength away from  $v=2$ . The peak at a lower field is barely visible at a small filling  $v = \sim 0.6$ , and it grows as  $v$  is increased and eventually results in “M” shaped displacement field dependence at half filling  $v = 2$  (Fig.3d and Fig.S11). For  $v>2$ , the relative strength of these two peaks are reversed, and instead it is the higher field peak whose intensity quickly diminished away from half filling (Fig.S11 and Fig.S12). Surprisingly, these peaks are found following the boundary of the halo structure in Fig. 3f. These observations suggest the “M” feature already emerges weakly when TDBG is tuned to the halo but strongly enhanced near  $v=2$ . The same behaviors are also observed in  $1.33^\circ$  device (Fig. S5d).

The “M” shaped field dependence of  $A_1$  at half filling  $v=2$  is strongly linked with the emergence of correlated insulating states. We plot the  $A_1$  and  $R$  together in Fig. 3d, and it’s intriguing to find that the two peaks of the ‘M’ feature locate exactly at the field where correlated insulating states start to emerge. As the twist angle is increased to  $1.42^\circ$  (Fig. S13, middle panel), where correlated insulating states are present yet not well developed, a feature of two peaks is still visible. It totally disappears at  $1.55^\circ$  (Fig. S13, bottom panel), where no signature of CI are found. However, the valley of “M” shaped  $A_1$  is unlikely related to the correlated gap opening, since it persists in the metallic halo regime (Fig. S10 and S11).

The peaks that envelop the halo structure are intimately connected to critical points of the spontaneous symmetry breaking. We plot the Hall coefficient,  $R_{\text{Hall}}=[R_{xy}(+B)-R_{xy}(-B)]/2B$ , together with  $A_1$  in Fig. 3e and Fig.S14. The  $A_1$  peaks are found concurrent with a sharp change of  $R_{\text{Hall}}$ . The sharp change of Hall coefficient demonstrates the critical point between symmetry broken state and conventional metal, in agreement with the observations in literature<sup>27</sup>.

**Discussion of critical behaviors and possible origins.** Beside the observation of an intimate connection between the enhanced T-linear resistivity and the critical points of symmetry broken states at the halo boundary, we show in the Figure 4 that such phase transitions at the critical points are continuous. Fig. 4a shows the  $R(T)$  curves at  $v = 2$  with applied field  $D$  in the vicinity of halo boundary. Taking the  $R(T)$  at  $D/\varepsilon_0 = -0.276$  V/nm for example, it displays insulating behavior for  $T < T^*$ , and reveals a metallic state with T-linear resistivity when  $T > T^*$ . Here,  $T^*$  serves as a critical temperature separating insulator/metal, and also it acts as the onset temperature for the T-linear regime. As the field is decreased,  $T^*$  gradually gets smaller and smaller, and it eventually disappears, i.e. approaches our base temperature of  $\sim 1.8$  K, at the boundary of halo structure with  $D/\varepsilon_0 = -0.2$  V/nm. The  $T^*$  are plotted in the phase diagram Fig. 4d with a domed shape. Meanwhile, thermal activation gaps of the insulators

at low temperature are extracted and plotted in Fig. S15. The vanishing gap and  $T^*$  at the boundary of halo structure suggest a continuous phase transition at the critical points, indicated by the cyan arrows in Fig.4d. Similarly, for  $R(T)$  curves at the filling  $v=1.8$  in Fig. 4b,  $T^*$  can be defined as a critical temperature, below which it is a symmetry broken metal and above which it is a metal with  $T$ -linear resistivity. And again,  $T^*$  is vanishing at the critical points, indicated by the cyan arrows in the Fig. 4e. Such a  $T$ -linear resistivity with  $T^*$  approaching the base temperature is a characteristic quantum critical behavior.

Outside the halo structure, the resistivity follows  $R \sim A_2 T^2$  dependence at  $T < T^*$  and  $R \sim A_1 T$  at  $T > T^*$ , as shown in Fig. 4c and Fig. S16. Here,  $T^*$  is the critical temperature separating  $T$ -square and  $T$ -linear dependence,  $A_1$  is the slope of  $T$ -linear resistivity, and  $A_2$  is the coefficient of  $T^2$  term that scales with effective mass in the Landau Fermi liquid theory. System with quantum critical point should show a divergence of  $A_2$  at critical point, indicating the failure of Fermi liquid model. The electric field dependent  $T^*$  and  $A_2$  are plotted in Fig. 4f-g. And once again, we find vanished  $T^*$  when approaching the critical displacement field. Besides,  $A_2$  tends to diverge at the critical points, suggesting diverging effective mass there.

The vanishing  $T^*$  and the diverging effective mass at the critical points are characteristics of quantum critical behavior. Moreover, we find the large  $T$ -linear resistivity falls into the regime where the Planckian dissipation dominates with  $\hbar/\tau = Ck_B T$  and  $C$  approaching  $O(1)$ . In twisted graphene moiré system<sup>21</sup>, the number  $C$  can be extracted from  $T$ -linear resistivity slope  $A_1$  by  $C = \hbar e^2 n A_1 / k_B m^*$ . In our cases, we obtain the  $C \sim 1.8$  for the  $A_1$  peaks at  $v=2$  in Fig. 3d, by taking  $m^* = 2.733 \times 10^{-31} \text{ kg}$ ,  $n = 1.75 \times 10^{16} / \text{m}^2$ ,  $A_1 = 146 \Omega / \text{K}$ . Last but not least, signs of linear in magnetic field ( $B$ ) resistivity are also revealed in Fig. S17, similar to a breakdown of quasiparticle picture in cuprate<sup>36</sup>. However, the linear range in  $B$  is quite limited, and more investigation are demanded in future. Taking all these facts into consideration, we tend to attribute the observed maximized  $T$ -linear resistivity at the boundary of halo structure to the quantum criticality.

At these critical points, quantum fluctuations are generated as a result of the competing between different phases (ground states). In TDBG, it is 4-fold degenerate outside the halo structure while it is 2-fold or even non-degenerate inside<sup>27</sup>. The boundary of the halo structure separate states with different symmetry, and is likely to bring about a symmetry-breaking instability. These fluctuations could drive the  $T$ -linear resistance all the way from ground state at low temperature up to high temperature where all these fragile and delicate ground states disappear (Fig.4 and Fig.S18). More specifically, we suspect it is the fluctuations from the spin degree of freedom<sup>37</sup> that contribute the quantum criticality. This is based on the unbalanced spin distribution inside and outside the halo. While spin-up electrons and spin-down electrons are equally filled outside the halo, one spin flavor is more favored than the other inside the halo structure, as demonstrated in the literature<sup>25</sup>.

Retrospectively, we suspect that the strange offset between  $R$  and  $A_1$  for  $1.55^\circ$  device in Fig. 2f where correlated insulating states absent is of the same origin. That is to say the strange metal behavior in Fig.2f suggests a more subtle and possible symmetry-broken ground states buried at a lower temperature. Indeed, signatures of halo and correlated insulating states are observed at a slightly smaller twist angle of  $1.53$  degree in the literature<sup>25</sup>. Thus, one would expect the  $T$ -linear resistivity at high temperature provides information of ground states at low temperature. However, more

investigations are expected in the future for a better understanding experimentally and theoretically.

Finally, we make a comparison of T-linear resistivity with different twist angle and displacement field in Figure 5. At  $D/\varepsilon_0 = 0$  V/nm, there is no correlated state regardless of twist angle, and the el-ph model (black dashed lines) gives a good description for the measured T-linear resistivity (purple circles). At  $D/\varepsilon_0 = -0.4$  V/nm, the phonon model still give a good description for large twist angles ( $>1.5^\circ$ ), however, it fails to account for the large T-linear slope for optimal twist angle ( $<1.5^\circ$ ) where correlated states and halo structures emerge. The failure of el-ph model in the correlated regime is in line with the rising of quantum criticality at the critical points of symmetry broken phase transition.

**Conclusions.** We systematically investigate the carrier density, displacement field and twist angle dependences of T-linear resistivity in TDBG. We demonstrate a dominant role played by acoustic phonons when correlated states are absent. The T-linear resistivity has a non-monotonic displacement field dependence with a single  $A_1$  peak related to vHS, revealing the field-tunable electron phonon interaction in TDBG. Moreover, we find features that beyond the phonon model in the presence of correlated states near optimal twist angle. Instead of a single peak, it is a “M” shaped two peak structure. These peaks are found located at the boundary of the halo structure, separating states with different symmetry. We attribute the observations to a consequence of fluctuations due to quantum criticality. The interpretation is supported by the facts of continuous phase transition, vanishing  $T^*$ , and the diverging effective mass at the critical points. Our observations establish a close link between high temperature T-linear resistivity to low temperature ground states, and would inspire more works about the nature of quantum criticality and ground states instability in TDBG. And similar analysis may also work in other field-tunable systems such as twisted monolayer-bilayer graphene<sup>38-40</sup> and ABC-stacking trilayer graphene/hBN moiré system<sup>41</sup>.

## Methods

**Sample fabrications.** Bilayer graphene flakes are exfoliated from highly oriented pyrolytic graphite, with the layer number determined by optical contrast and further confirmed by atomic force microscope. Thermal annealing is performed to ensure the stacking order of bilayer graphene to be Bernal stacking and remove contaminations on exfoliated graphene and hBN surfaces. Samples are assembled by “cut-and-stack” method technique using Poly Bisphenol A carbonate film coating on a polydimethyl siloxane stamp placed on a glass slide. The twist angle is controlled by a rotator stage with accuracy  $0.02^\circ$ . After the pick-up procedure, the obtained heterostructure is transferred onto silicon slice with 300nm silicon dioxide. Heterostructures are fabricated into Hall bar devices through electron beam lithography and reactive ion etching with  $\text{CHF}_3/\text{O}_2$  as reactive gas, and contacted by Cr/Au through electron beam evaporation system. Heavily doped silicon or few layer graphite are used as bottom gate and Ti/Au metal film as top gate, respectively.

**Electrical measurements.** Devices are measured in a helium-4 vapor flow cryostat (1.8K) with a standard lock-in technique. Typical a.c. current is applied by Stanford SR830 with a low frequency of 30.9Hz and a current of 10nA. Temperature is controlled by Cryo Con 32B PID temperature controller with long enough delay time to ensure thermal equilibrium in the device.

**Linear fit procedures.** We refer to the linear fit slope as “ $A_1$ ” and local numerical differential as

“dR/dT” for distinction. Linear fit is done by utilizing “ployfit” function in numpy library of Python. The temperature range for linear fit is checked manually from individual R-T curves to avoid artifacts owing to insensitivity of the linear correlation coefficient. Besides, local numerical differential of R-T curves is done to check the correctness of the linear fit. The local numerical differential is based on three-point Lagrange numerical differential formula programed on Python.

**Electron-phonon scattering model.** For el-ph scattering model simulation, the effective mass near  $1.3^\circ$  is referred to Ref. 25, being  $0.3m_e$ . From continuum model calculations, we get conduction moiré bandwidth (BW) at different twist angles. Then, by  $m^*(\theta)=m^*(1.3^\circ)\times BW(1.3^\circ)/BW(\theta)$ , we get  $m^*$  at  $1.42^\circ$ ,  $1.55^\circ$ ,  $1.91^\circ$ , and eventually obtain  $v_F = \sqrt{(\hbar^2 n \pi/2)/m^*}$ . Taking  $\rho_m=7.6\times 10^{-7}\text{kg/m}^2$ ,  $v_{ph}=2.1\times 10^4\text{m/s}$ ,  $U=21\text{eV}$ ,  $z_\infty=1.5$ , we can get the T-linear slope dependence on  $n$  at certain twist angle. As for twist angle dependence of T-linear slope by el-ph scattering, the  $m^*(\theta)$  is linear fitted by known  $m^*$  at certain twist angles. We use  $U=25\text{eV}$ ,  $z_\infty=1.55$ , relatively larger values than carrier density dependence simulation, however, the el-ph predictions are still smaller than the experimental data near  $1.3^\circ$ , as shown in Fig. 5. The electron phonon scattering model is programmed on Python.

**Others.** For the field dependent  $A_1$  at a filling close to  $v=2$ , the peaks can be identified directly from the “M” shaped plots. For the field dependent  $A_1$  at a filling away from  $v=2$ , one peak is prominent while the other is very faint, giving a shoulder like structure. We identify the faint one by subtracting a linear background of the shoulder feature. The linear background is defined by linking the two side-turning-points of the shoulder.

## Data availability

The data that support the findings of this study are available from the corresponding authors upon reasonable request.

## Reference

- 1 Ziman, J. M. *Electrons and phonons: the theory of transport phenomena in solids.* (Oxford university press, 2001).
- 2 Varma, C. M. Colloquium: Linear in temperature resistivity and associated mysteries including high temperature superconductivity. *Reviews of Modern Physics* **92**, 031001, doi:10.1103/RevModPhys.92.031001 (2020).
- 3 Coleman, P. & Schofield, A. J. Quantum criticality. *Nature (London)* **433**, 226-229 (2005).
- 4 Sachdev, S. & Keimer, B. Quantum criticality. *Physics today* **64**, 29 (2011).
- 5 Keimer, B., Kivelson, S. A., Norman, M. R., Uchida, S. & Zaanen, J. From quantum matter to high-temperature superconductivity in copper oxides. *Nature (London)* **518**, 179-186 (2015).
- 6 Shibauchi, T., Carrington, A. & Matsuda, Y. A quantum critical point lying beneath the superconducting dome in iron pnictides. *Annu. Rev. Condens. Matter Phys.* **5**, 113-135 (2014).
- 7 Zhou, R. *et al.* Quantum criticality in electron-doped BaFe  $2-x$  Ni  $x$  As 2. *Nature communications* **4**, 1-7 (2013).

8 Gegenwart, P., Si, Q. & Steglich, F. Quantum criticality in heavy-fermion metals. *nature physics* **4**, 186-197 (2008).

9 Stewart, G. Non-Fermi-liquid behavior in d-and f-electron metals. *Reviews of modern Physics* **73**, 797 (2001).

10 Shen, B. *et al.* Strange-metal behaviour in a pure ferromagnetic Kondo lattice. *Nature (London)* **579**, 51-55 (2020).

11 Cano-Cortes, L., Merino, J. & Fratini, S. Quantum critical behavior of electrons at the edge of charge order. *Physical review letters* **105**, 036405 (2010).

12 Sato, T. *et al.* Strange metal from a frustration-driven charge order instability. *Nature materials* **18**, 229-233 (2019).

13 Bistritzer, R. & MacDonald, A. H. Moire bands in twisted double-layer graphene. *Proceedings of the National Academy of Sciences of the United States of America* **108**, 12233-12237, doi:10.1073/pnas.1108174108 (2011).

14 Cao, Y. *et al.* Correlated insulator behaviour at half-filling in magic-angle graphene superlattices. *Nature* **556**, 80-84, doi:10.1038/nature26154 (2018).

15 Cao, Y. *et al.* Unconventional superconductivity in magic-angle graphene superlattices. *Nature* **556**, 43-50, doi:10.1038/nature26160 (2018).

16 Yankowitz, M. *et al.* Tuning superconductivity in twisted bilayer graphene. *Science* **363**, 1059-1064, doi:10.1126/science.aav1910 (2019).

17 Lu, X. *et al.* Superconductors, orbital magnets and correlated states in magic-angle bilayer graphene. *Nature* **574**, 653-657, doi:10.1038/s41586-019-1695-0 (2019).

18 Sharpe, A. L. *et al.* Emergent ferromagnetism near three-quarters filling in twisted bilayer graphene. *Science* **365**, 605-608, doi:10.1126/science.aaw3780 (2019).

19 Serlin, M. *et al.* Intrinsic quantized anomalous Hall effect in a moire heterostructure. *Science* **367**, 900-903, doi:10.1126/science.aay5533 (2020).

20 Polshyn, H. *et al.* Large linear-in-temperature resistivity in twisted bilayer graphene. *Nature Physics* **15**, 1011-1016, doi:10.1038/s41567-019-0596-3 (2019).

21 Cao, Y. *et al.* Strange Metal in Magic-Angle Graphene with near Planckian Dissipation. *Physical Review Letters* **124**, 076801, doi:10.1103/PhysRevLett.124.076801 (2020).

22 Bruin, J. A. N., Sakai, H., Perry, R. S. & Mackenzie, A. P. Similarity of Scattering Rates in Metals Showing T-Linear Resistivity. *Science* **339**, 804-807, doi:10.1126/science.1227612 (2013).

23 Wu, F., Hwang, E. & Das Sarma, S. Phonon-induced giant linear-in-T resistivity in magic angle twisted bilayer graphene: Ordinary strangeness and exotic superconductivity. *Physical Review B* **99**, 165112, doi:10.1103/PhysRevB.99.165112 (2019).

24 Cao, Y. *et al.* Tunable correlated states and spin-polarized phases in twisted bilayer-bilayer graphene. *Nature* **583**, 215-220, doi:10.1038/s41586-020-2260-6 (2020).

25 Liu, X. *et al.* Tunable spin-polarized correlated states in twisted double bilayer graphene. *Nature* **583**, 221-225 (2020).

26 Shen, C. *et al.* Correlated states in twisted double bilayer graphene. *Nature Physics* **16**, 520-525 (2020).

27 He, M. *et al.* Symmetry breaking in twisted double bilayer graphene. *Nature Physics* **17**, 26-30, doi:10.1038/s41567-020-1030-6 (2020).

28 Burg, G. W. *et al.* Correlated Insulating States in Twisted Double Bilayer Graphene. *Physical Review Letters* **123**, 197702, doi:10.1103/PhysRevLett.123.197702 (2019).

29 Wu, F. & Das Sarma, S. Ferromagnetism and superconductivity in twisted double bilayer graphene. *Physical*

*Review B* **101**, 155149, doi:10.1103/PhysRevB.101.155149 (2020).

30 Saito, Y., Ge, J., Watanabe, K., Taniguchi, T. & Young, A. F. Independent superconductors and correlated insulators in twisted bilayer graphene. *Nature Physics* **16**, 926–930 (2020).

31 Efetov, D. K. & Kim, P. Controlling electron-phonon interactions in graphene at ultrahigh carrier densities. *Phys Rev Lett* **105**, 256805, doi:10.1103/PhysRevLett.105.256805 (2010).

32 Betz, A. C. *et al.* Supercollision cooling in undoped graphene. *Nature Physics* **9**, 109–112, doi:10.1038/nphys2494 (2012).

33 Song, J. C., Reizer, M. Y. & Levitov, L. S. Disorder-assisted electron-phonon scattering and cooling pathways in graphene. *Phys Rev Lett* **109**, 106602, doi:10.1103/PhysRevLett.109.106602 (2012).

34 Li, X., Wu, F. & Das Sarma, S. Phonon scattering induced carrier resistivity in twisted double-bilayer graphene. *Physical Review B* **101**, 245436 (2020).

35 Wallbank, J. R. *et al.* Excess resistivity in graphene superlattices caused by umklapp electron-electron scattering. *Nature Physics* **15**, 32–36, doi:10.1038/s41567-018-0278-6 (2018).

36 Giraldo-Gallo, P. *et al.* Scale-invariant magnetoresistance in a cuprate superconductor. *Science* **361**, 479–481, doi:10.1126/science.aan3178 (2018).

37 Moriya, T. & Ueda, K. Spin fluctuations and high temperature superconductivity. *Advances in Physics* **49**, 555–606, doi:10.1080/000187300412248 (2000).

38 Chen, S. *et al.* Electrically tunable correlated and topological states in twisted monolayer–bilayer graphene. *Nature Physics*, doi:10.1038/s41567-020-01062-6 (2020).

39 Polshyn, H. *et al.* Electrical switching of magnetic order in an orbital Chern insulator. *Nature*, doi:10.1038/s41586-020-2963-8 (2020).

40 Xu, S. *et al.* Tunable van Hove singularities and correlated states in twisted monolayer–bilayer graphene. *Nature Physics*, doi:10.1038/s41567-021-01172-9 (2021).

41 Chen, G. *et al.* Evidence of a gate-tunable Mott insulator in a trilayer graphene moire superlattice. *Nature Physics* **15**, 237–241, doi:10.1038/s41567-018-0387-2 (2019).

## Acknowledgements

We thank Rui Zhou, S. Das Sarma, Xi Dai, Hongming Weng, Jianpeng Liu, Lede Xian, Xiao Li for helpful discussions. This work was supported by the National Key Research and Development Program (Grant No. 2020YFA0309600), the NSFC (Grants Nos. 61888102, 11834017, and 12074413), the Strategic Priority Research Program of CAS (grant Nos.XDB30000000 and XDB33000000), the Key-Area Research and Development Program of Guangdong Province (Grant No.2020B0101340001), and the Research Program of Beijing Academy of Quantum Information Sciences under Grant No. Y18G11. Growth of hexagonal boron nitride crystals was supported by the Elemental Strategy Initiative conducted by the MEXT, Japan, Grant Number JPMXP0112101001, JSPS KAKENHI Grant Number JP20H00354 and A3 Foresight by JSPS.

## Author contributions

W.Y. and G.Z. supervised the project. Y.C., C.S., W.Y., and G.Z. conceived the experiments. Y.C., L.L. and C.S. fabricated the devices and performed the transport measurements. Y.C., L.L. and J.T. provided the samples. L.L. provided continuum model calculations. K.W. and T.T. provided hexagonal boron nitride crystals. Y.C., W.Y., and G.Z. analyzed the data. Y.C. and W.Y. wrote the paper. All authors discussed and commented on this work.

## Competing interests

The authors declare no competing interests.

## Figure captions

**Figure 1. Schematics of T-linear resistivity originated from (a) electron-phonon scattering and (b) quantum critical point (QCP).** The Bloch-Grüneisen temperature ( $T_{BG}$ ) is defined when Fermi momentum  $k_F$  is half of the maximum phonon wave vector  $q$ , and  $\alpha>1$  is the power law coefficient when  $T < T_{BG}$ .

**Figure 2. T-linear resistivity and field-tunable electron-phonon interactions in 1.55° TDBG.** (a) Resistivity ( $R$ ) as a function of carrier density ( $n$ ) and displacement field ( $D$ ) at  $T=1.8$ K. Charge neutral point, single-particle superlattice gaps on electron and hole branches are marked by CNP,  $+n_s$ , and  $-n_s$ , respectively. (b) Line cuts of  $R(T)$  at  $D/\varepsilon_0=0$ V/nm for  $\nu$  from 0.5 to 2.5, with a step of 0.5, and  $\varepsilon_0$  is the vacuum permittivity. (c) Extracted linear slope  $A_1(n)$  at  $D/\varepsilon_0=0$ V/nm (blue solid line), and corresponding el-ph simulation (orange dash line). We set the error bar of the simulation to 40%, mainly due to the uncertainty of acoustic phonon deformation potential and effective mass. (d) Line cuts of  $R(T)$  at  $\nu=2$  for  $D/\varepsilon_0$  from 0 to -0.7V/nm, with a step of 0.1V/nm. The positions of these  $R$ - $T$  curves in (b) and (d) are marked as colored dots in (a). (e) Extracted  $A_1$  as a function of displacement field at  $\nu=0.5, 1, 1.5$  and  $2$ , with an offset of  $5\Omega/K$  for clarity. The light blue dash arrow illustrates the shift of  $A_1$  peak with decreasing  $\nu$ . (f) Zoom-in plot of (a). Black dash lines mark the weak cross structure and yellow dots mark the position where  $A_1$  maximizes.

**Figure 3. Correlation of maximized T-linear resistivity and the symmetry broken phase transition at the boundaries of the halo structure in 1.23° TDBG.** (a) Mapping of  $R(n, D/\varepsilon_0)$  at

$T=1.8\text{K}$ . **(b-c)** Line cuts of  $R(T)$  at  $v=2$  **(b)** and  $v=1.8$  **(c)** with  $D/\varepsilon_0$  changes from  $-0.1$  to  $-0.6\text{V/nm}$ . **(d)** The comparison between  $A_1$  and  $R$  at  $v=2$ , where  $R$  is measured at  $T=1.8\text{K}$ . These vertical dash lines mark the position of  $A_1$  peaks, also fits well with the critical points between conventional metal (labelled by 'M') and correlated insulator (labelled by 'CI'). **(e)** A comparison between  $A_1$  and Hall coefficient at  $v=1.8$ . Hall signals are measured at  $T=1.8\text{K}$  with a magnetic field of  $B=0.1\text{T}$  to minimize any influence on zero-field band structure. These vertical dash lines are eye guides for  $A_1$  peak positions, which also matches the critical points between conventional metal (labelled by 'M') and symmetry broken metal (labelled by 'SBM'). **(f)** Zoom-in of the resistivity as a function of  $v$  and  $D/\varepsilon_0$  in  $1.23^\circ$  device. Yellow (black) dots mark the  $A_1$  peak position at high (low) displacement field.

**Figure 4. Quantum critical behaviors at the boundaries of halo structures in  $1.23^\circ$  TDBG.** **(a-b)** Line cuts of  $R(T)$  near critical points at  $v=2$  **(a)** and  $v=1.8$  **(b)**. There is an offset of  $200\ \Omega$  between curves in **(b)** for clarity. **(c)** Line cuts of  $R(T)$  outside the halo at  $v=2$ .  $T^*$  indicated by the black arrows in **(a-c)** is the characteristic temperature defined in the main text. The blue dash lines are  $T^2$  dependence fitted by experimental curve at  $T < T^*$ . The pink lines show the  $T$ -linear resistivity at  $T > T^*$ . **(d-e)** Mappings of local numerical  $dR/dT(D, T)$  at  $v=2$  **(d)** and  $v=1.8$  **(e)**, respectively. The  $T^*$  are marked by black dots. The upper temperature boundaries of  $T$ -linear resistivity are marked by yellow dots. The cyan arrows indicate the critical points, and 'CI', 'M' and 'SBM' are referred to correlated insulator, conventional metal, symmetry broken metal, respectively. The temperature range in **(d-e)** is  $1.8\text{K}$  to  $30\text{K}$ . **(f-g)**  $A_2$  and  $T^*$  as a function of displacement field at  $v=2$  **(f)** and  $v=1.8$  **(g)**. The black arrows indicate the critical points, and the grey areas are the regime of correlated ground states inside the halo.

**Figure 5. Comparison of experimental  $A_1$  and el-ph simulations at different twist angles.** The dark blue dash line shows the el-ph simulations with twist angle dependent effective mass. Here,  $z_\infty=1.55$ ,  $U=25\text{eV}$ , Fermi velocity is calculated at  $n=2\times 10^{12}/\text{cm}^2$ . The el-ph simulation error bar is 40%.

## Figures

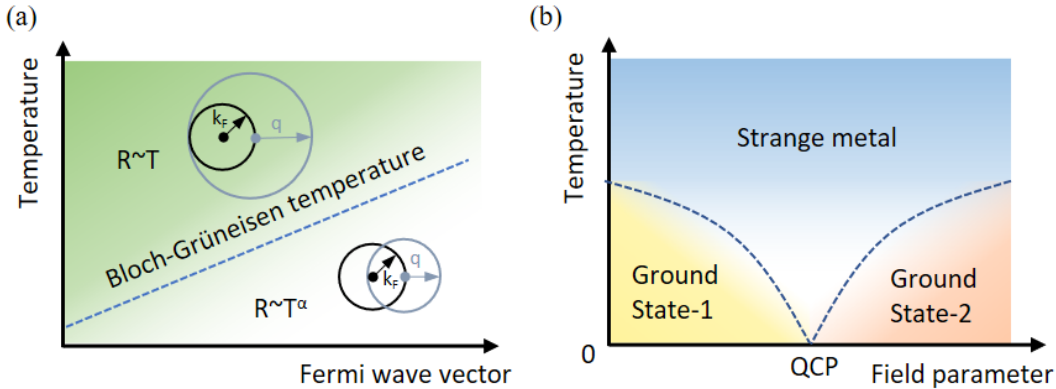


**Figure 1**

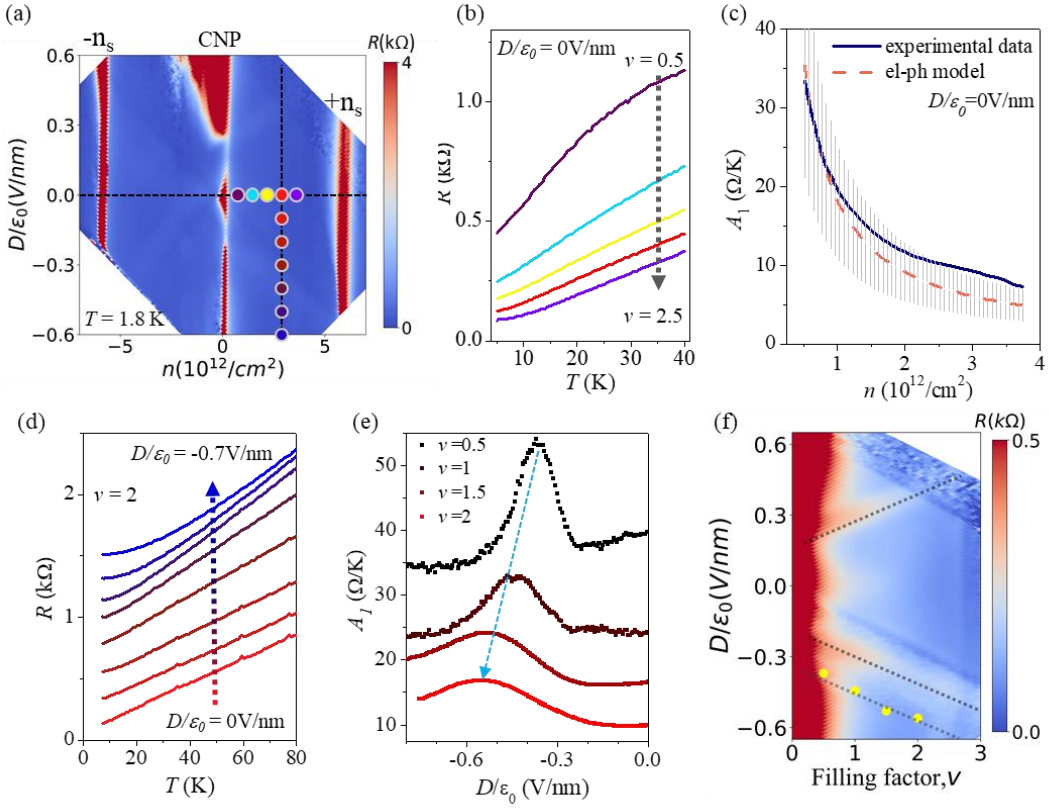


**Figure 2**

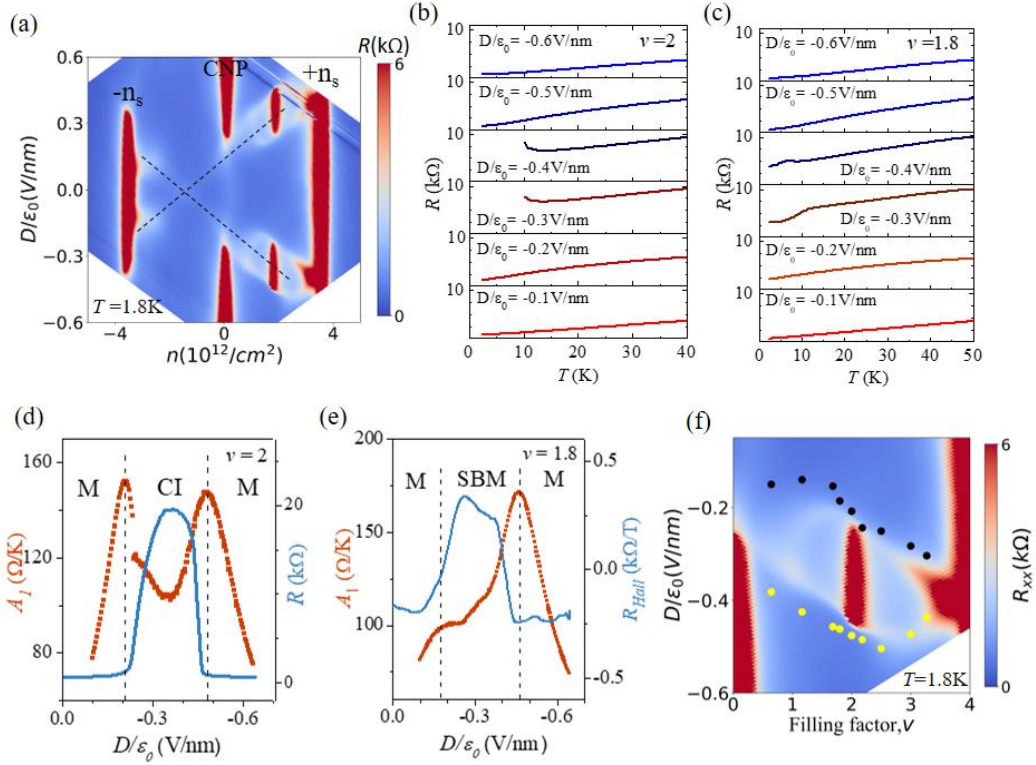


**Figure 3**

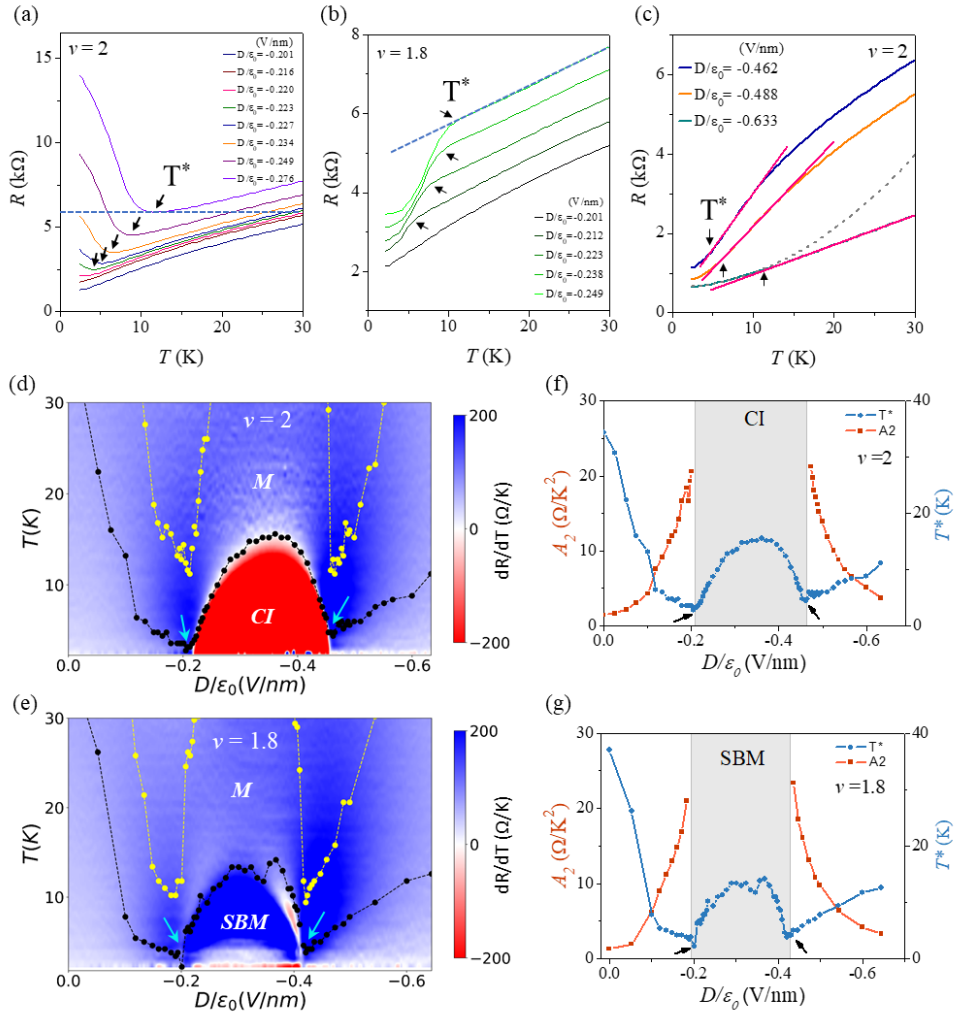


**Figure 4**

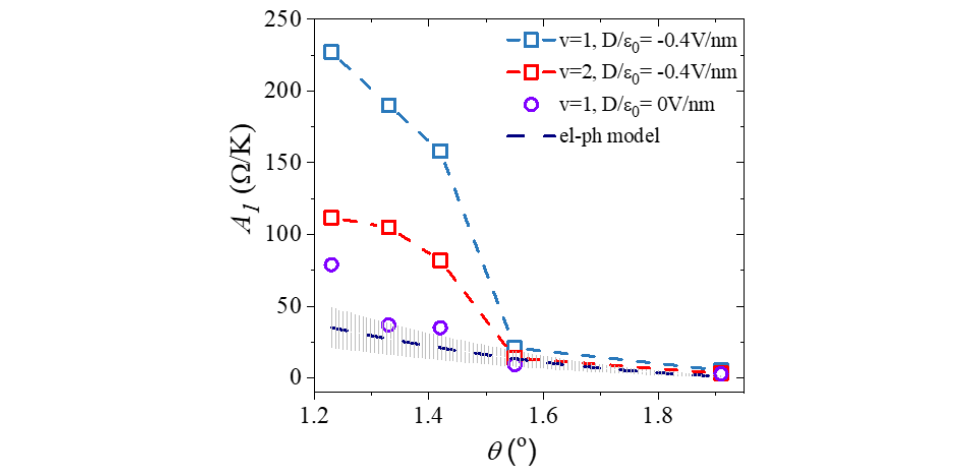
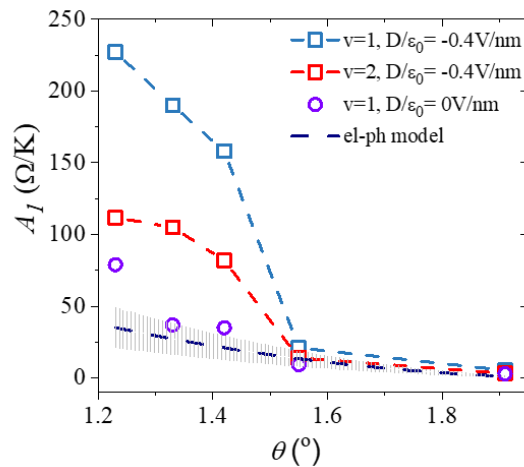


**Figure 5**



## Supplementary information

### I. Band structure calculation of twisted double bilayer graphene

TDBG is composed by two Bernal stacked bilayers and there is a tiny twist angle between them. We label each layer carbon atoms A<sub>1</sub>, B<sub>1</sub>, A<sub>2</sub>, B<sub>2</sub>, A<sub>3</sub>, B<sub>3</sub>, A<sub>4</sub>, B<sub>4</sub>, where 1-4 represent top layer to bottom layer and A, B represent sublattice indices<sup>[1]</sup>.

We can construct the lattice structure of bilayer graphene before the rotation.  $\mathbf{a}_1 = a \left( \frac{1}{2}, -\frac{\sqrt{3}}{2} \right)$ ,  $\mathbf{a}_2 = a \left( \frac{1}{2}, \frac{\sqrt{3}}{2} \right)$  are the lattice vectors, where  $a \approx 0.246\text{nm}$ . According to the lattice vectors, we can define the reciprocal vectors,  $\mathbf{a}_1^* = (2\pi/a) \left( 1, -\frac{1}{\sqrt{3}} \right)$ ,  $\mathbf{a}_2^* = (2\pi/a) \left( 1, \frac{1}{\sqrt{3}} \right)$ . In our calculation, the top layer is rotated clockwise by  $\frac{\theta}{2}$ , and the bottom layer is rotated anticlockwise by  $\frac{\theta}{2}$ . After the rotation, reciprocal vectors are  $\mathbf{a}_i^{*(l)} = R \left( \mp \frac{\theta}{2} \right) \mathbf{a}_i^*$ , where  $l = 1, 2$  represent top and bottom layer. Dirac points in graphene are located at  $\mathbf{K}_\xi^{(l)} = -\xi [\mathbf{a}_1^{*(l)} + \mathbf{a}_2^{*(l)}]/3$ , where  $\xi = \pm 1$  represents valley index.

Using the effective low energy continuum model<sup>[1,2]</sup>, we construct the Hamiltonian in the basis of Bloch states of AB stacked graphene, which can be expressed in second quantization formulation:  $\psi_{k_1 k_2}^T = (C_{A1}(k_1), C_{B1}(k_1), C_{A2}(k_1), C_{B2}(k_1), C_{A3}(k_2), C_{B3}(k_2), C_{A4}(k_2), C_{B4}(k_2))$ . Hamiltonian can be expressed by

$$\begin{pmatrix} H_0(\mathbf{k}_1) & g^\dagger(\mathbf{k}_1) & 0 & 0 \\ g(\mathbf{k}_1) & H'_0(\mathbf{k}_1) & T^\dagger & 0 \\ 0 & T & H_0(\mathbf{k}_2) & g^\dagger(\mathbf{k}_2) \\ 0 & 0 & g(\mathbf{k}_2) & H'_0(\mathbf{k}_2) \end{pmatrix} + V \quad (1)$$

Where  $\mathbf{k}_l = R(\pm\theta/2)(\mathbf{k} - \mathbf{K}_\xi^{(l)})$ , and

$$H_0(\mathbf{k}) = \begin{pmatrix} 0 & -\hbar v_0 k_- \\ -\hbar v_0 k_+ & \Delta \end{pmatrix}, \quad (2)$$

$$H'_0(\mathbf{k}) = \begin{pmatrix} \Delta & -\hbar v_0 k_- \\ -\hbar v_0 k_+ & 0 \end{pmatrix}, \quad (3)$$

$$g(\mathbf{k}) = \begin{pmatrix} \hbar v_4 k_+ & \gamma_1 \\ \hbar v_3 k_- & \hbar v_4 k_+ \end{pmatrix}, \quad (4)$$

Where  $k_\pm = \xi k_x \pm ik_y$ ,  $\hbar v_i = (\sqrt{3}/2)\gamma_i a$ , we use the parameters from ref.<sup>[3]</sup>

$$(\gamma_0, \gamma_1, \gamma_3, \gamma_4, \Delta) = (2610, 361, 283, 138, 15)\text{meV} \quad (5)$$

$\gamma_0$  is intralayer nearest-neighbor hopping term,  $\gamma_1$  is interlayer hopping term in bilayer graphene, from bottom layer A sublattice to top layer B sublattice.  $\gamma_3$  will bring trigonal warping to this system, which could increase the bandwidth of low energy band.  $\gamma_4$  and  $\Delta$  make the valence band and conductance band asymmetrical, which is called electron-hole asymmetry.

The interlayer coupling between the two layers twisted relatively is

$$T(\mathbf{r}) = T_1 + T_2 e^{i\xi \mathbf{G}_1^M \cdot \mathbf{r}} + T_3 e^{i\xi \mathbf{G}_2^M \cdot \mathbf{r}} \quad (6)$$

$$T_1 = \begin{pmatrix} w_{AA} & w_{AB} \\ w_{AB} & w_{AA} \end{pmatrix}, \quad T_2 = \begin{pmatrix} w_{AA} & w_{AB} e^{-i\xi\varphi} \\ w_{AB} e^{i\xi\varphi} & w_{AA} \end{pmatrix}, \quad T_3 = \begin{pmatrix} w_{AA} & w_{AB} e^{i\xi\varphi} \\ w_{AB} e^{-i\xi\varphi} & w_{AA} \end{pmatrix} \quad (7)$$

Where  $\varphi = 2\pi/3$ ,  $\mathbf{G}_i^M = \mathbf{a}_i^{*(1)} - \mathbf{a}_i^{*(2)}$  ( $i = 1, 2$ ), representing moiré reciprocal lattice vector. We set  $w_{AA} = 50\text{meV}$ ,  $w_{AB} = 85\text{meV}$  for adapting to our system, Mainly due to slightly larger angle  $1.55^\circ$  and the relaxation effect<sup>[4]</sup>.

TDBG is electric field adjustable. In our calculation, V represents on-site energy of every layer when the system is subjected to a perpendicular external electric field.

$$V = \begin{pmatrix} \frac{3}{2}U\hat{1} & 0 & 0 & 0 \\ 0 & \frac{1}{2}U\hat{1} & 0 & 0 \\ 0 & 0 & -\frac{1}{2}U\hat{1} & 0 \\ 0 & 0 & 0 & -\frac{3}{2}U\hat{1} \end{pmatrix} \quad (8)$$

Where U is electrostatic potential energy of each layer, and  $\hat{1}$  is a  $2 \times 2$  unit matrix. Given a wave vector  $\mathbf{k}$ , there are many states at  $\mathbf{k} + m\mathbf{G}_1^M + n\mathbf{G}_2^M$  engaging in the interlayer scattering, where the range of integer m and n is  $[-N, N]$ . In our calculation, N is truncation value and assigned 4, so the dimensional of matrix is  $2 \times 4 \times (2N + 1)^2 = 648$ .

## Reference:

- [1] M. Koshino. Band structure and topological properties of twisted double bilayer graphene. *Phys. Rev. B* **99**, 235406 (2019).
- [2] R. Bistritzer and A. H. MacDonald. Moiré bands in twisted double-layer graphene. *Proceedings of the National Academy of Sciences* **108**, 12233 (2011).
- [3] Jung, J. & MacDonald, A. H. Accurate tight-binding models for the  $\pi$  bands of bilayer graphene. *Phys. Rev. B* **89**, 035405 (2014).
- [4] M. Koshino, N. F. Q. Yuan, T. Koretsune, M. Ochi, K. Kuroki, and L. Fu. Maximally Localized Wannier Orbitals and the Extended Hubbard Model for Twisted Bilayer Graphene. *Phys. Rev. X* **8**, 031087 (2018)

## II. Extended data

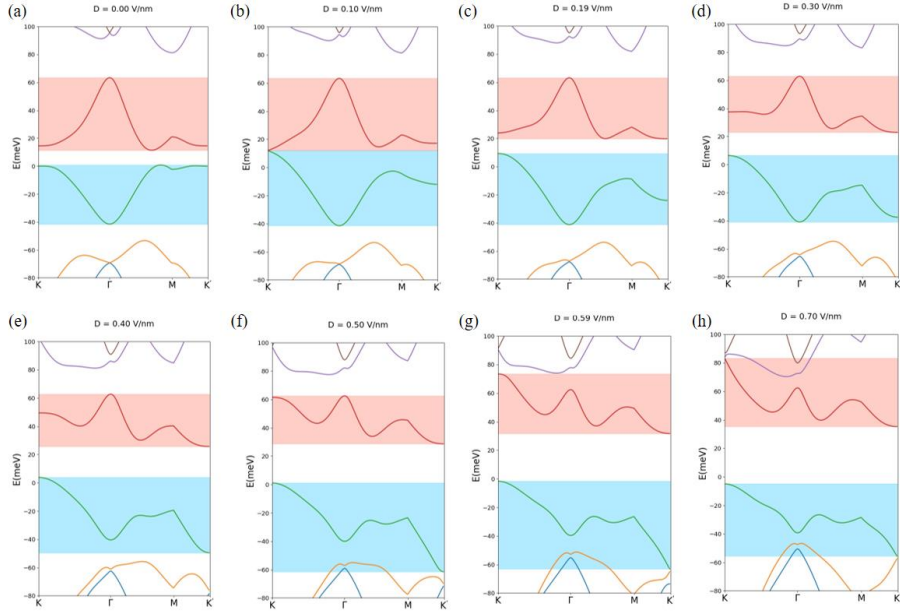


**Figure S1. Effect of electric field on calculated band structure for 1.55°.** (a-h) Calculated band structure for 1.55° TDBG based on full parameter continuum model with electric field uniformly distributed across the four layers.

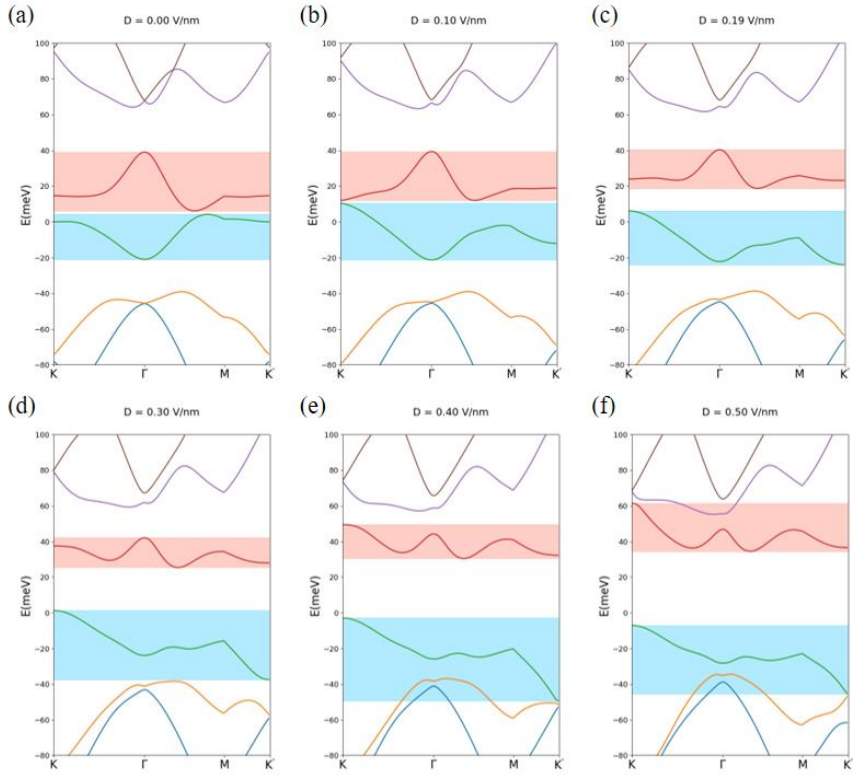


**Figure S2. Effect of electric field on calculated band structure for 1.33°.** (a-f) Calculated band structure for 1.33° TDBG based on full parameter continuum model with electric field uniformly distributed across the four layers.

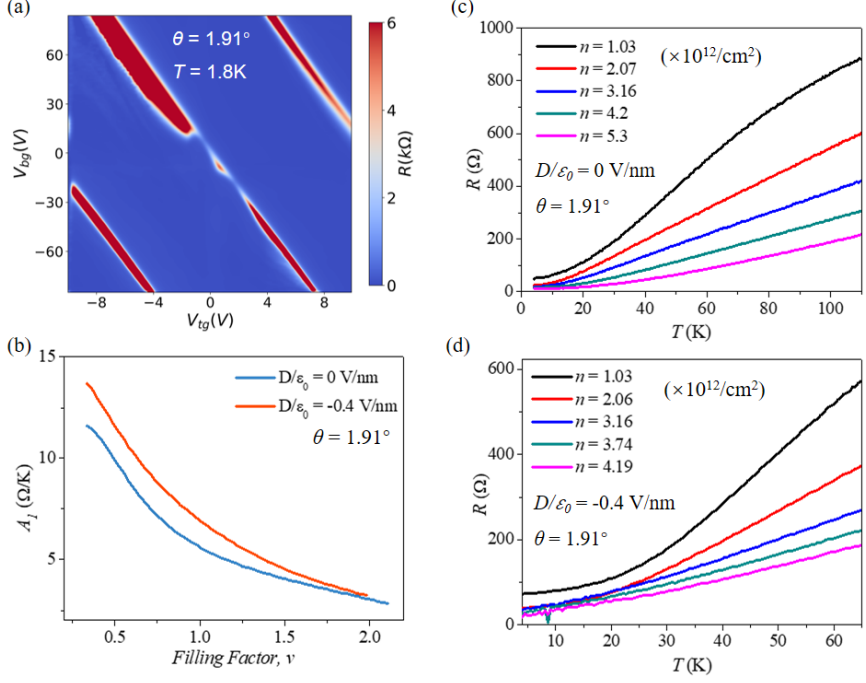


**Figure S3. T-linear resistance behavior in 1.91° device.** (a) Resistance as a function of  $V_{tg}$  and  $V_{bg}$ . (b)  $A_1$  as a function of  $v$  at  $D/\epsilon_0=0$  V/nm (dark blue) and  $D/\epsilon_0=-0.4$  V/nm (orange). (c-d) Resistance as a function of  $T$  at  $D/\epsilon_0=0$  V/nm (c) and  $D/\epsilon_0=-0.4$  V/nm (d).

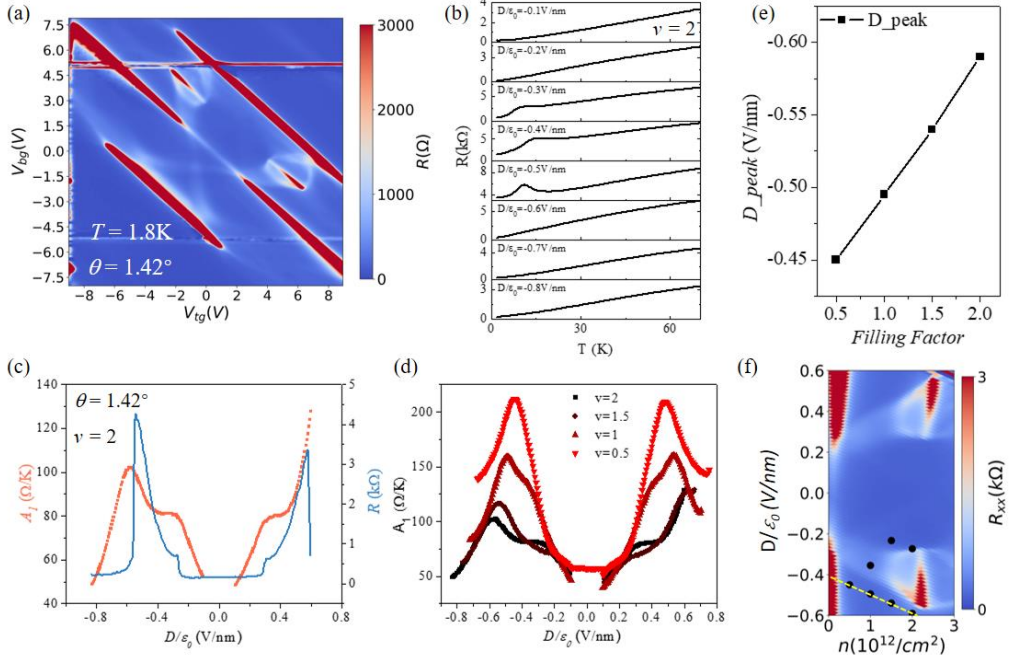


**Figure S4. T-linear resistance behavior for 1.42° TDBG.** (a) Resistance as a function of  $V_{tg}$  and  $V_{bg}$ . (b) Resistance as a function of  $T$  at  $v=2$  with  $D/\epsilon_0$  step of 0.1 V/nm. (c)  $A_1$  and resistance as a function of  $D/\epsilon_0$  at  $v=2$ . (d)  $A_1$  as a function of  $D/\epsilon_0$  at various  $v$ . (e) The displacement field of the  $A_1$  peak as a function of  $v$ . (f) Zoom in of the resistance as a function of  $v$  and  $D/\epsilon_0$  in 1.42° device. Black dots mark the position of the  $A_1$  peak, yellow dash line is the linear guide line for the eye.

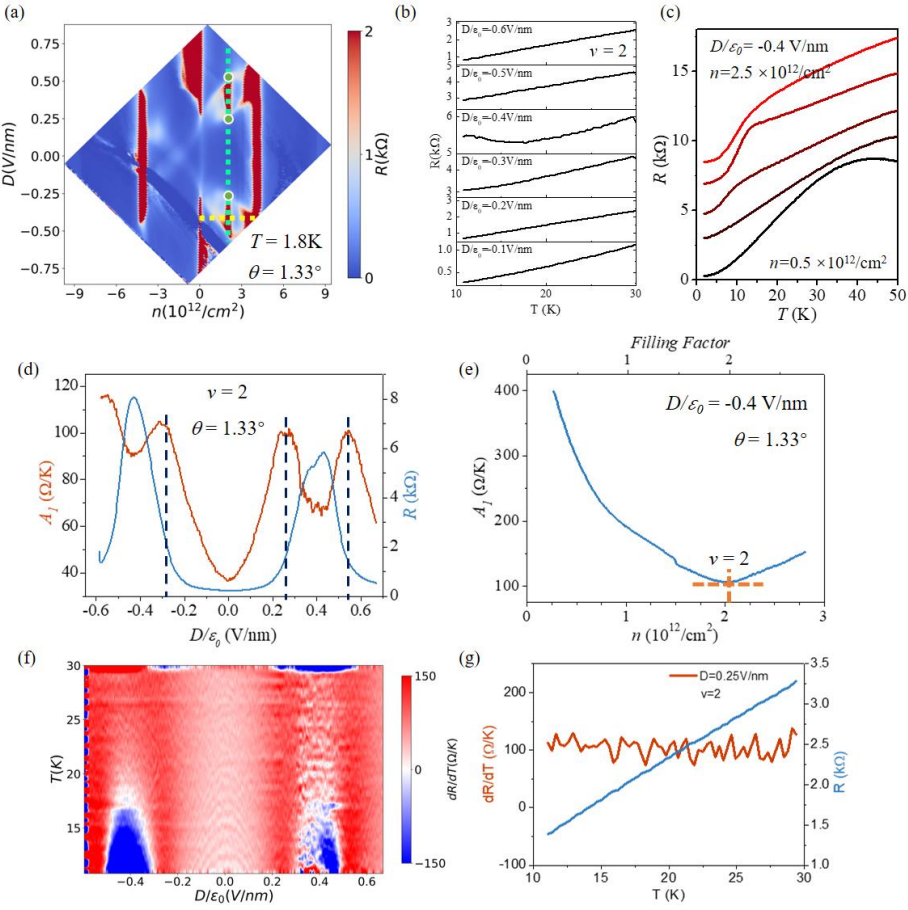


**Figure S5. T-linear resistance behavior for 1.33° TDBG.** (a) Resistance as a function of carrier density and displacement field in 1.33° device. (b-c) Resistance as a function of temperature at  $\nu=2$  (b) and  $D/\epsilon_0=-0.4V/nm$  (c). (d)  $A_1$  and resistance as a function of displacement field at  $\nu=2$ . (e)  $A_1$  as a function of carrier density at  $D/\epsilon_0=-0.4V/nm$ . (f) numerical derivate  $dR/dT$  as a function of displacement field and temperature at  $\nu=2$ . (g) Resistance and numerical  $dR/dT$  as a function of temperature near critical points at  $\nu=2$ , obtained from (f).

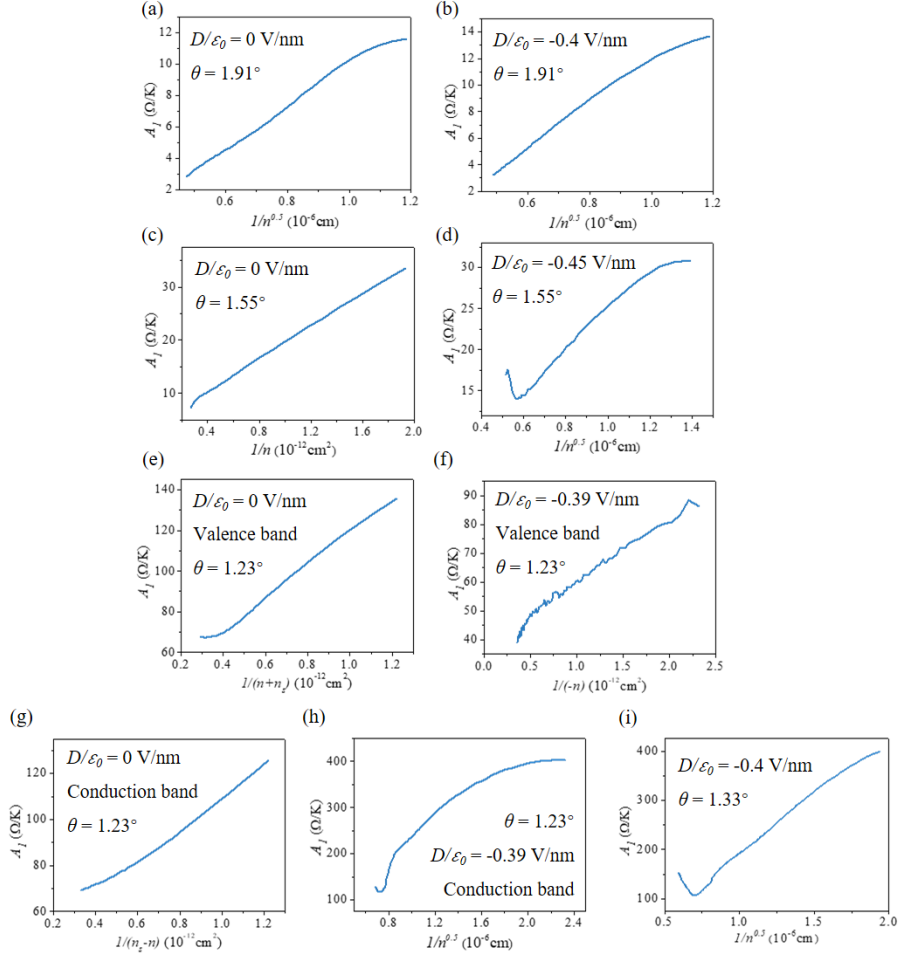


**Figure S6. Carrier density scaling of  $A_1$ .** For larger twist angle devices ( $1.55^\circ$  and  $1.91^\circ$ ), the  $A_1$  scales linearly with  $1/\sqrt{n}$  in (a-b,d), while scales with  $1/n$  at  $D/\varepsilon_0=0\text{V}/\text{nm}$  in  $1.55^\circ$  device in (c). The different scaling of  $1/n$  or  $1/\sqrt{n}$  may root in field and twist angle tunable band structure in TDBG. For  $1.23^\circ$  device, (e,g) at  $D/\varepsilon_0=0\text{V}/\text{nm}$ , the  $A_1$  is linear in  $1/n$  as well in both CB and VB. Here,  $n$  is relative value to full filling of moiré conduction ( $+n_s$ ) and valence ( $-n_s$ ) band, respectively. At  $D/\varepsilon_0=-0.39\text{V}/\text{nm}$ , (f)  $A_1$  is linear with  $1/n$  in valence band. (h) But neither  $1/n$  nor  $1/\sqrt{n}$  can well capture the linear dependence of  $A_1$  in conduction band. On the contrary, (i)  $A_1$  obtained from  $1.33^\circ$  device at the similar displacement field shows  $1/\sqrt{n}$  scaling of  $A_1$ .

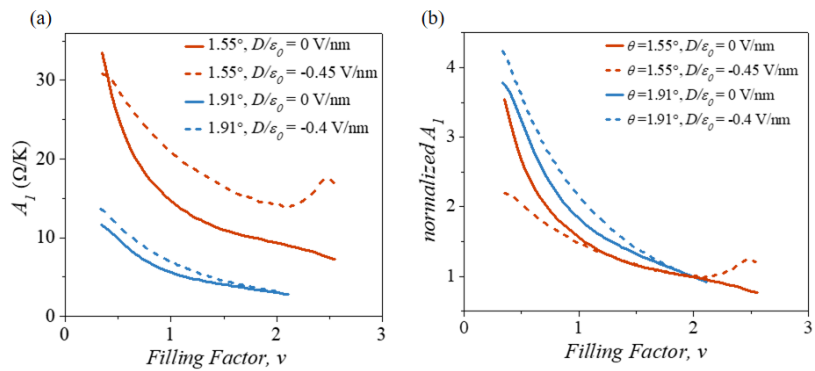


**Figure S7. Extracted  $A_1$  as a function of  $v$  for larger twist angle devices.** (a) Extracted  $A_1$  as a function of  $v$  in  $1.55^\circ$  and  $1.91^\circ$  device. (b) Normalized  $A_1(v)/A_1(v=2)$ .

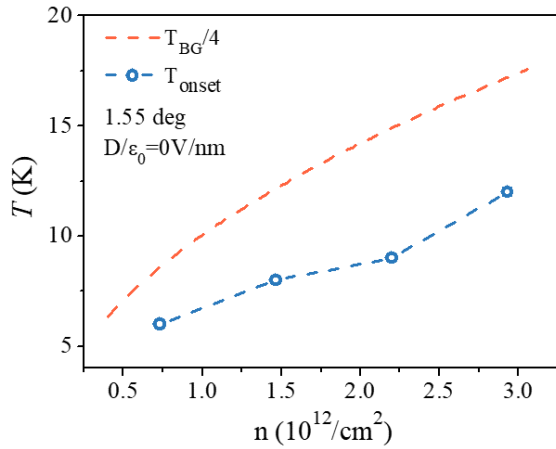


**Figure S8. Bloch-Grüneisen temperature ( $T_{BG}$ ) and experimental T-linear onset temperature ( $T_{onset}$ ) for  $1.55^\circ$  device at  $D/\epsilon_0=0V/nm$ .**

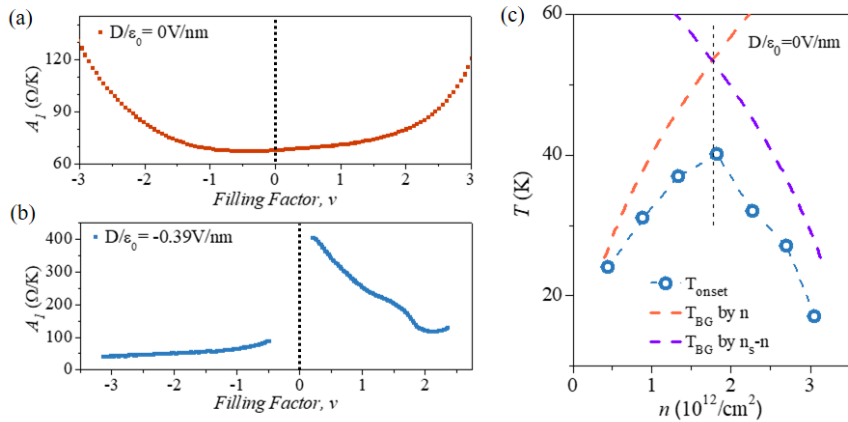


**Figure S9. Carrier density dependence of  $A_1$  in  $1.23^\circ$  TDBG. (a-b)**  $A_1$  as a function of  $v$  at  $D/\epsilon_0=0V/nm$  (a) and  $D/\epsilon_0=-0.39V/nm$  (b). For  $1.23^\circ$  device, because the overall smaller bandwidth of conduction band (CB) and valence band (VB), the T-linear resistance is observed in both electron and hole branches. At  $D/\epsilon_0=0V/nm$ , the gap closing at CNP brings the conduction and valence moiré band together. At  $D/\epsilon_0=-0.39V/nm$ , the CNP gap opening separates the CB and VB. (c) Comparison between  $T_{onset}$  and  $T_{BG}$  at  $D/\epsilon_0=0V/nm$  in the conduction band.  $T_{onset}$  maximizes at  $v=2$ , and follows the trend of  $T_{BG}$  calculated based on  $n$  (or  $n_s-n$ ) at  $v<2$  ( $v>2$ ).

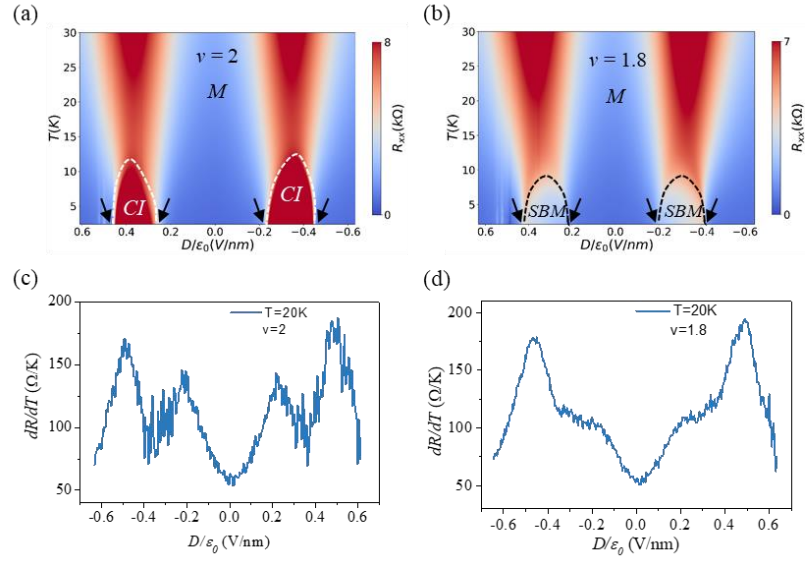


**Figure S10. Local numerical differential  $dR/dT$  in  $1.23^\circ$  TDBG.** (a-b) Mappings of  $R(D,T)$  at  $\nu=2$  (a) and  $\nu=1.8$  (b). 'CS', 'M' and 'SBS' refer to correlated insulating states, conventional metal, symmetry broken states, respectively. (c-d) Numerical  $dR/dT$  as a function of  $D/\varepsilon_0$  at  $T=20K$  for  $\nu=2$  (c) and  $\nu=1.8$  (d). It's clear that 'M' shape feature and shoulder-like feature preserves. The numerical differential can rule out effect of averaging by linear fit, confirming the experimental observations in the main text.

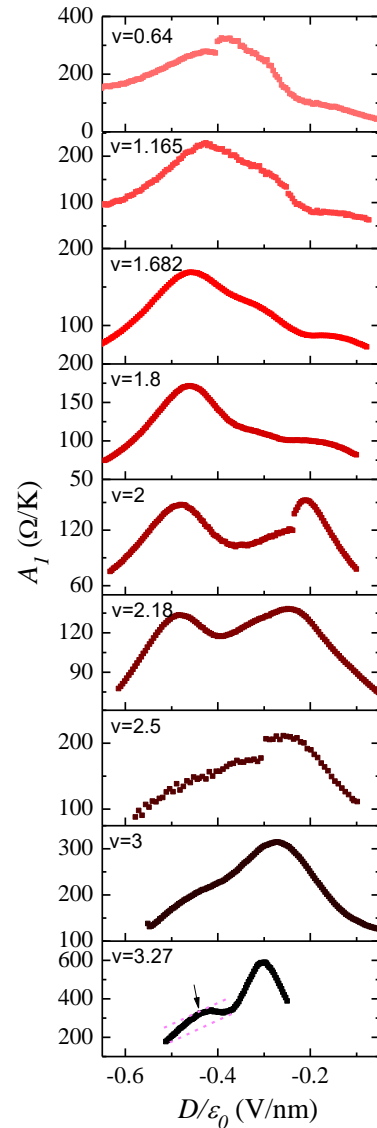


**Figure S11.  $A_1$  as a function of displacement field at various  $v$  in 1.23° TDBG.** The red dashed lines at the bottom subfigure are used to identify the faint peak (indicated by the black arrow) from the shoulder structure.

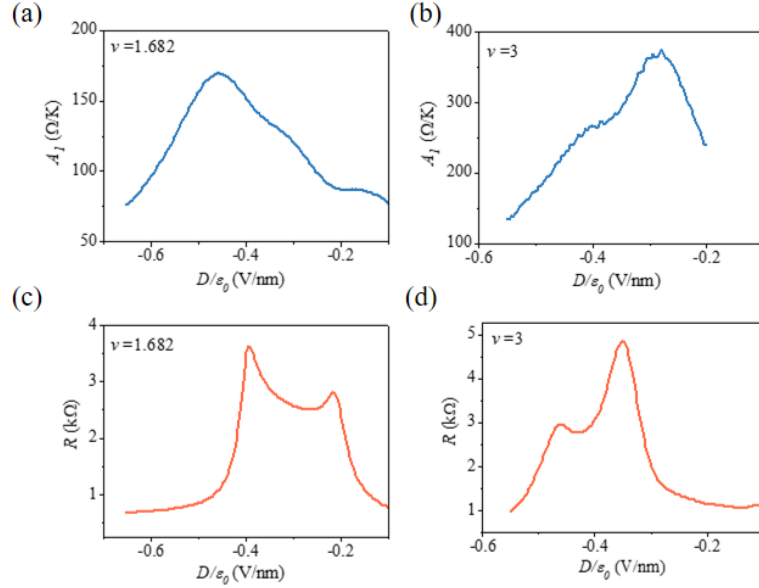


**Figure S12. The correlation between the intensity of  $A_1$  peak and halo boundaries in  $1.23^\circ$  TDBG. (a-b)**  
 $A_1$  as a function of displacement field at  $\nu=1.682$  (a) and  $\nu=3$  (b). (c-d) Resistance as function of displacement field at  $\nu=1.682$  (c) and  $\nu=3$  (d),  $T=1.8K$ . It's clear that the stronger  $A_1$  peak always locates near the more intensive halo boundary.

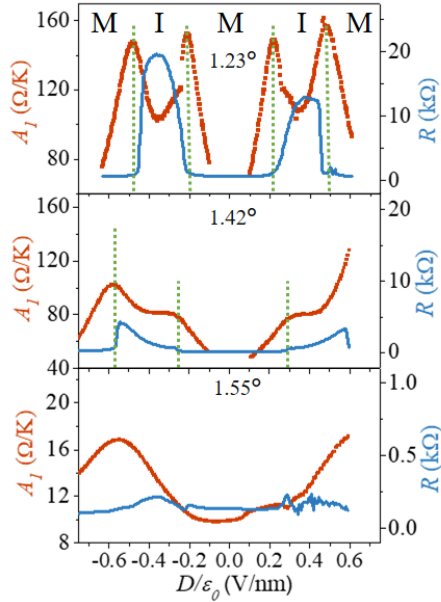


**Figure S13. Twist angle dependence of  $A_1$  as a function of  $D/\epsilon_0$ .**  $A_1$  and resistance measured at base temperature as a function of displacement field at  $\theta=1.23^\circ$  (top panel),  $1.42^\circ$  (middle panel),  $1.55^\circ$  (bottom panel) at  $\nu=2$ . Link between the 'M' feature and correlated insulating states can be confirmed.

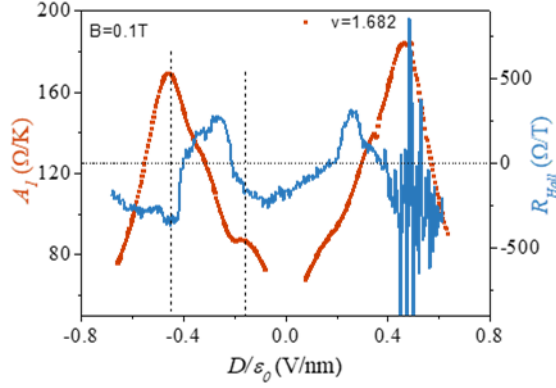


**Figure S14. The correlation between the non-symmetric peak and critical points in 1.23° TDBG.**  $A_1$  and Hall resistance as a function of displacement field at  $\nu=1.682$ . Hall resistance are measured at  $B=0.1T$ . The vertical dash lines mark the positions of  $A_1$  peaks, which locate near the abrupt change of Hall resistance.

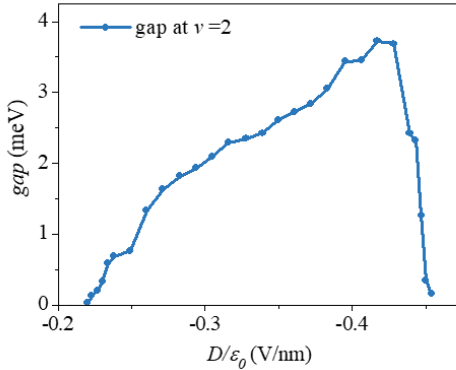


**Figure S15. Continuous closing of gap at critical points at  $\nu=2$  in 1.23° TDBG.** Thermal excitation gap at  $\nu=2$  as a function of displacement field.

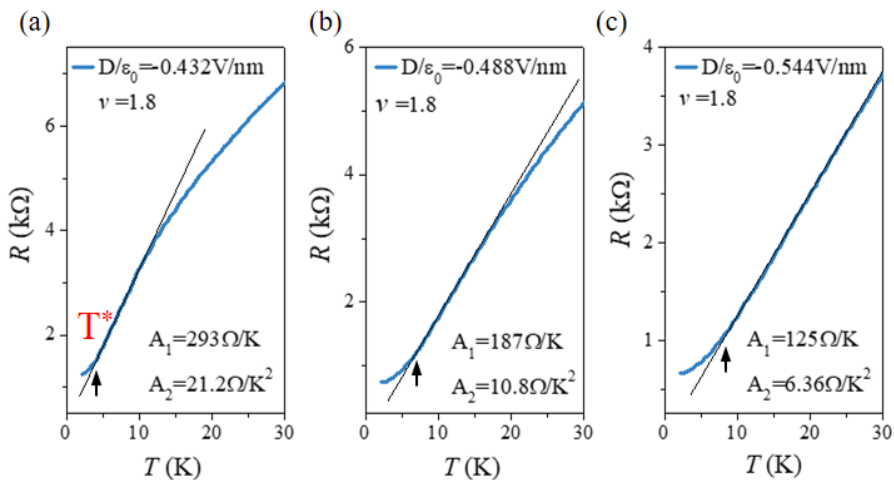


**Figure S16. T-linear and T-square resistivity transition outside the halo in 1.23° TDBG.** (a-c) Resistance as a function of temperature at  $\nu=1.8$  at selected displacement fields. The black arrows mark the  $T^*$ , which is the upper boundary for  $R \sim T^2$  and lower boundary for  $R \sim T$ . The fitted  $A_1$  and  $A_2$  is shown in corresponding figures.

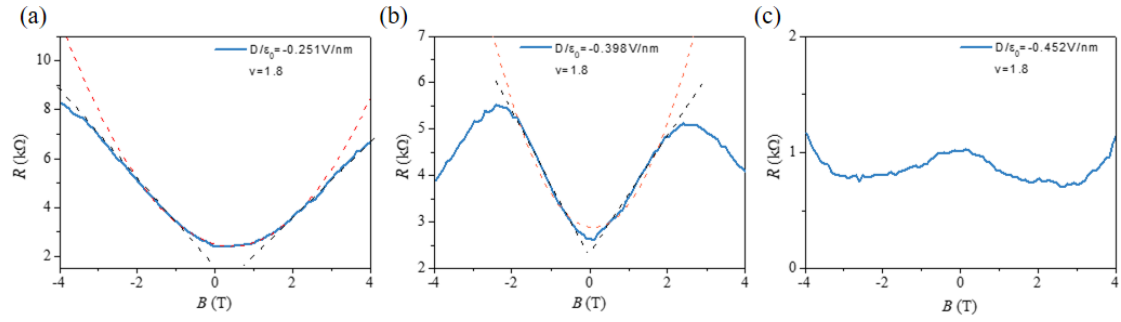


**Figure S17. Magnetoresistance at  $v=1.8$  in  $1.23^\circ$  TDBG. (a-c)** resistance as a function of vertical magnetic field at  $D/\epsilon_0 = -0.251 \text{ V/nm}$  (a),  $-0.398 \text{ V/nm}$  (b),  $-0.452 \text{ V/nm}$  (c). The black and red dashed lines indicate  $B$ -linear and  $B$ -square dependence, respectively. Signature of  $B$ -linear resistance is observed but the range in  $B$  is quite limited.

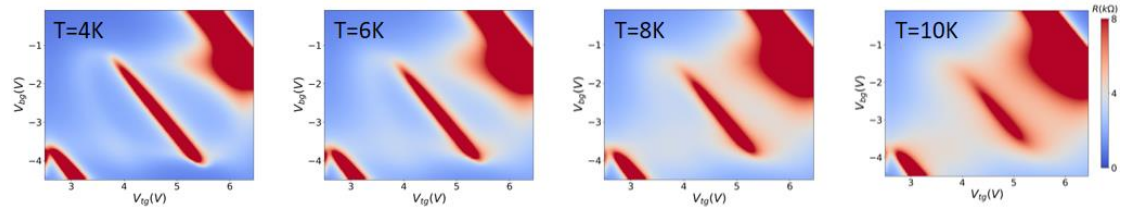


**Figure S18. Temperature dependence of the halo structure in  $1.23^\circ$  TDBG.** At  $T=8 \text{ K}$ , the halo structure has already been hard to distinguish.